

A proposal of urban coastal pattern for improving pedestrian wind comfort in coastal cities

Journal of Building Physics

1–31

© The Author(s) 2023

Article reuse guidelines:

sagepub.com/journals-permissions

DOI: 10.1177/17442591231177429

journals.sagepub.com/home/jen

Hakan Baş¹ , İlknur Türkseven Doğrusoy² and Sigrid Reiter³

Abstract

High-speed wind flow in urban areas poses a risk of pedestrian wind discomfort. Coastal cities, particularly, are at risk of wind discomfort as they are exposed to strong sea breezes. To improve the wind climate in coastal cities, we redesigned a standard coastal urban fabric by placing a new building at its center. Then we investigated the effect of critical variables, the central building's location (x/L ratio) and dimensions (*height, width, length*) on wind conditions with a parametric design approach based on the computational fluid dynamics (CFD) method validated by experimental data. We found that an optimum combination of x/L ratio and central building height (H) can reduce the *corner* and *double corner effect* between two parallel buildings by up to 45% and minimize the risk of wind discomfort. The findings can be applied to newly-designed coastal settlements where wind shelter is required and can help urban policymakers and designers.

Keywords

Urban coastal pattern, coastal city, pedestrian wind comfort, sea breeze, computational fluid dynamics (CFD)

¹Department of Architecture, Faculty of Engineering and Architecture, İzmir Katip Çelebi University, İzmir, Turkey

²Department of Architecture, Faculty of Architecture, Dokuz Eylül University, İzmir, Turkey

³LEMA – Local Environment Management and Analysis, University of Liège, Liège, Belgium

Corresponding author:

Hakan Baş, Department of Architecture, Faculty of Engineering and Architecture, İzmir Katip Çelebi University, Balatçık Mahallesi, Havaalani Şosesi, No:33/2 Balatçık 35620 Çiğli, İzmir, Turkey.

Email: hakan.bas@ikc.edu.tr



Figure 1. Trees which are bent due to the prevailing sea breeze (a) Karşıyaka Promenade, Izmir, Turkey (author's photo) and (b) Sea Point Promenade, Cape Town, South Africa (Google Earth, accessed 14 June 2021).

Introduction

High-rise and large buildings in cities cause high-speed wind flow that creates disturbing physical effects on pedestrians and reduces pedestrian wind comfort in urban open spaces (Stathopoulos and Blocken, 2016). Coastal cities, particularly, coastal passages between two parallel buildings are most at risk of wind discomfort (Johansson and Yahia, 2020; Szűcs, 2013) since they are exposed to open and high-speed sea breeze which generally acts from the front side to the seafront buildings. The risk of wind discomfort in passages adversely affects coastal city life and reduces the quality of urban living. Despite the positive effects of the sea breezes in reducing the stagnated heat in urban areas (Lim and Ooka, 2021), improving urban air quality (Chen et al., 2021) and thermal comfort with a cooling effect on hot summer days (Dürr et al., 2023), the high-speed sea breezes can increase building heat losses in cold climates (Thébault and Millet, 2017) and can cause the risk of pedestrian wind discomfort (Szűcs, 2013). Although sea breezes are not high-speed in some coastal cities, the existing built environment can increase the speed of sea breezes, creating a risk of wind discomfort.

Seafront buildings are the place where the wind first penetrates the urban fabric. The first interaction between the seafront buildings and the wind causes the wind to accelerate. Therefore, in coastal cities, the urban fabric should be adapted to the sea breeze and particular attention should be paid to the urban coastal pattern for a comfortable urban life.

In coastal cities, the sea generally is the source of the wind. The sea breeze blows from the sea to the land. The speed of the sea breeze increases as the temperature difference between the sea and the land increases. Figure 1(a) and (b) show the trees bent under the strong influence of sea breezes that blow throughout the year. This observation shows that the urban fabric should be designed taking into account the direction of the sea breeze.

Regarding wind comfort in urban settlements, many computational wind studies have been conducted on the most common flow types around basic components of a city, such as street canyons, courtyards, and block archetypes (Melbourne and Joubert, 1971; Oke, 1988; Reiter, 2010; Steemers et al., 1997; Wise, 1970). Twelve basic aerodynamic effects around buildings were determined by Gandemer (1978), and the main flow characteristics around buildings of various shapes and different wind incidences were investigated by DeKay and Brown (2013). Beranek and Van Koten (1982) investigated wind speed conditions in passages between three parallel shifted buildings, and Blocken et al. (2007a) investigated wind speed conditions and various flow interactions in passages of varying widths between parallel buildings. With these studies, the *corner effect*, developing flow acceleration around the building corners (Gandemer, 1978), and the strong flow interactions in the central axis of passages between parallel buildings, the *double corner effect*, have been well documented (Blocken et al., 2007a).

The wind climate is directly dependent on the building geometry (shape, size, configuration). Many studies focused on finding ideal building geometries to achieve the ideal wind climate. The effect of building corner modification on wind conditions has been widely investigated (Bottema, 1993; Mittal et al., 2019; Stathopoulos, 1985; Xu et al., 2017). Bottema (1993) studied the basic shapes of building corners (chamfered, stepped, and rounded) to reduce the intensity of the *corner effect* and found that with the modified building corner shape, wind speed can be limited to 30% where the building heights are 50 m. Xu et al. (2017) studied aerodynamic corner modification using super-tall buildings of different shapes and found that the corner modification (corner chamfered and corner cut) reduced the acceleration area by approximately 30%. Bas et al. (2022) proposed an alternative design of urban seafront buildings based on a shifted building configuration that completely prevents the *double corner effect* in coastal passages where the building heights are 25 m. However, there is still limited motivation for how to create desired wind conditions in coastal urban environments. This may be due to the complexity of urban aerodynamics. A rather complex flow pattern is observed in urban environments, as buildings affect each other's flow field and cause flow interference and aerodynamic interaction. The fact that the buildings have a bluff body makes wind flow acceleration inevitable in urban places and makes it difficult to create ideal wind conditions.

Unlike many studies, this article focuses on minimizing the wind discomfort risk in coastal cities with open wind conditions, rather than wind flow analysis around buildings. Many strategies can be developed to reduce the risk of wind discomfort in the coastal passages between parallel buildings. The strategy tested in this article to improve the wind conditions of urban coastal settlements is to modify the front of a standard urban pattern (coastal pattern) by strategically placing a new central building between two parallel buildings on the passage center axis (PCA). This strategy aims to prevent the *corner* and *double corner effect* that develops in a passage between two parallel upwind buildings by using the central building as a wind-break. In this context, we investigated the optimum locations and dimensions

(height, width, length) of the central building, which will cause the least risk of wind discomfort with a parametric design approach.

When assessing the risk of wind discomfort at a site, it is recommended to consider 36 wind directions with 10° increments (City of London and RWDI, 2019). However, site-specific wind discomfort and safety probability study, which considers all wind directions by statistical method, is beyond the scope of this article. We aim to create a strategy and test the potential solutions for adapting urban front lines of coastal cities to the prevailing sea breezes; based on the assumption that the wind originates from the open sea. Therefore, we focused only on the prevailing sea breeze, as it is the most regular and the one that causes the most problems of wind discomfort in coastal cities.

The main contribution of this study is to develop alternative urban coastal patterns to minimize the risk of wind discomfort by using the parametric design and computational fluid dynamics (CFD) method. On the other hand, providing detailed explanations of CFD validation processes, with all calculations can help architects and urban planners to find solutions for a variety of pedestrian wind comfort problems by following the specified CFD process. In this context, this article also describes step-by-step the validation process of CFD for turbulent atmospheric boundary layer (ABL) while developing new urban coastal patterns. This study is expected to benefit many stakeholders. First, it will assist urban policy-makers in establishing wind-comfortable urban planning policies in coastal cities. Second, it will help architects and city planners to design wind-comfortable urban open areas.

The study is structured as follows. Section 2 presents the methodology, including the description of the proposed urban coastal patterns and urban geometric indicators, and then details the computational setup for simulations. Section 3 assesses the risk of wind discomfort of the proposed urban coastal patterns and Section 4 discusses the findings considering similar studies. Finally, Section 5 presents the conclusions.

Methodology

This study is based on a methodology that integrates the CFD method with the parametric design method. The CFD method provides a performance evaluation of proposed urban coastal patterns. It was specifically chosen as it is more practical for parametric design studies (van Hooff and Blocken, 2010) and it allows rapid testing of parametric urban models and visualization of the entire flow area (Blocken et al., 2011). For simulations, STAR-CCM+ which is a general-purpose CFD code was used and the CFD results were validated by experimental data.

Geometric description of urban coastal patterns

Acceleration of wind flow around buildings is inevitable as buildings often have sharp-edged bluff bodies. Specifically, narrow passages between parallel buildings

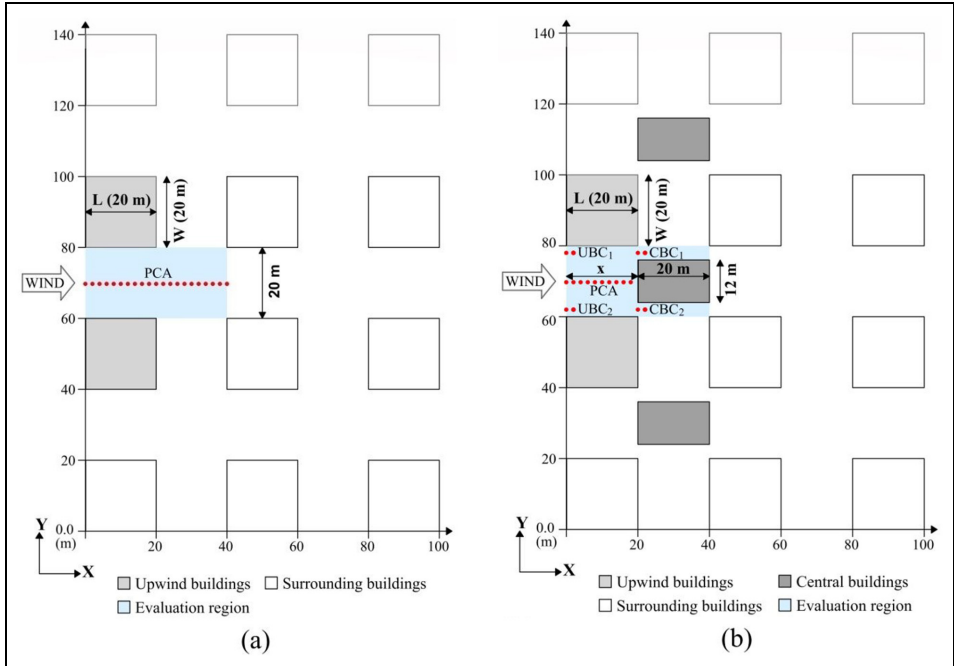


Figure 2. (a) Plan view of the standard urban pattern and data points and (b) plan view of the urban coastal pattern and data points, (PCA: passage center axis, CBC₁ and CBC₂: central building corner, UBC₁ and UBC₂: upwind building corner).

are the potential location of *strong flow interaction* and *double corner effect* (Blocken et al., 2007a; Reiter, 2010). The strategy to reduce the risk of wind discomfort between two parallel buildings in this study is to locate a new central building between parallel buildings. The critical questions are where to locate the new central building and what its dimensions should be. These questions constitute the form-making logic of hypothetical urban coastal patterns.

First, we created a standard urban pattern of 4×3 buildings of uniform height (20 m) with a street width of 20 m (Figure 2(a)). The scale ratio of the buildings is 1:1:1 (height: width: length). This standard urban pattern is used as the baseline model to create new urban coastal patterns.

The central building consists of a simple rectangular building with a 12 m width and 20 m length, and it is placed between two parallel upwind buildings in the standard urban pattern. The location of the central building is determined based on a single urban geometric indicator: x/L where x is the distance between the front edge of upwind buildings and the central building, and L is the length of the upwind buildings (Figure 2(b)).

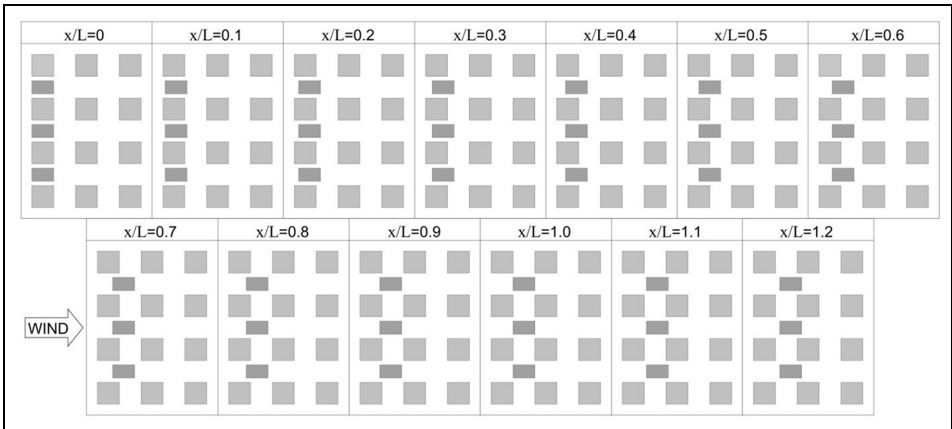


Figure 3. Plan view of the urban coastal patterns created according to 13 different x/L ratios.

For an accurate assessment of the wind climate, it is critical to accurately predict the potential location of the highest wind speeds in the evaluation region. According to the literature, critical locations are the areas where the *corner* and *double corner effect* occurs (Blocken et al., 2007a; Reiter, 2010). Therefore, data points are located 2 m apart on the passage center axis (PCA) and at the corners of the added central building (CBC_1 and CBC_2) and upwind buildings (UBC_1 and UBC_2) (Figure 2(b)). It should be noted that the location of the highest wind speeds may vary due to the geometrical difference of urban coastal patterns and may be located around the data points rather than above the assigned data points. Therefore, the data points on PCA, CBC, and UBC were assigned as the representative points to capture the highest wind speed. Based on the simulation results, the highest wind speed on or around the data points of PCA, UBC and CBC will be considered. At this point, we took the advantage of the CFD method, which allows the visualization of the entire flow area. In the test cases with x/L ratios between 0 and 0.3, the data points on UBC and CBC overlap. Therefore, only the data points from CBC are considered for these test cases. The corners of the surrounding buildings (upwind buildings) are another location where the wind flow accelerates, but we only considered the wind conditions at the inner passages. Data points were placed on PCA in the same configuration in the standard urban pattern (Figure 2(a)).

A total of 195 different urban coastal patterns were created using 13 ratios of x/L , from 0 to 1.2 with an increment of 0.1 and fifteen different building heights (H) from 2 to 30 m with an increment of 2 m. Figures 3 and 4 show the plan and front view of the urban coastal patterns, respectively.

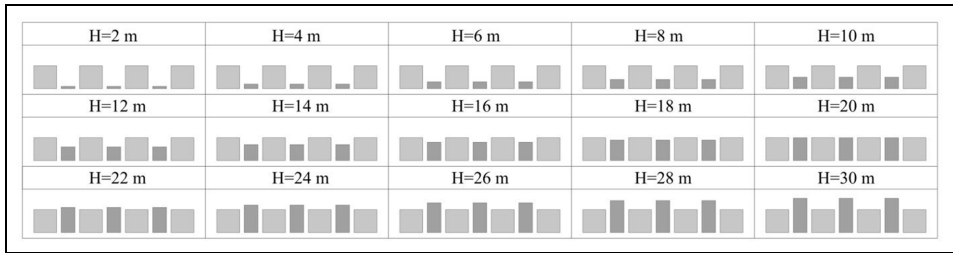


Figure 4. Front view of the urban coastal patterns created according to 15 different building heights (H).

CFD validation

CFD tools solve mathematical equations using numerical discretization. As computer power is still limited today, it is necessary to simplify equations to solve many flow problems. However, simplifying the equations can cause errors and uncertainties that often make CFD results inconsistent and unstable while reducing the computation time. To keep errors and uncertainties as small as possible, Best Practice Guidelines (BPGs) have been created for non-CFD experts that summarize the critical points of calculation parameters (Casey and Wintergerste, 2000; Franke et al., 2007; Tominaga et al., 2008). At all stages of the validation process, the CFD setup was created according to the BPGs. Two key goals, maximum predictive accuracy, and minimum computational run-time shaped the CFD process.

The CFD validation process begins with the acquisition of reliable experimental data. Calculating inflow parameters based on experimental data and the BPGs is a critical step in obtaining accurate results and keeping initial data uncertainty as low as possible (Franke et al., 2007). At this stage, velocity and turbulence quantities should be as close as possible to the experimental data. Choosing the appropriate turbulence model according to the character of the flow problem and optimum grid resolution is another critical step to achieving an acceptable result rapidly.

After determining the CFD setup parameters, it is useful to perform a simulation in an empty domain to check for *horizontal homogeneity* throughout the computational domain. According to Blocken et al. (2007b), horizontal homogeneity implies that the wind profile in the test area where the buildings would be positioned and the inlet wind profiles are the same. In a horizontally homogeneous flow, no streamwise gradients in the vertical profiles of the mean wind speed and turbulence quantities occur. It is also useful to check for reverse flow at the outlet. Simulation results may change if acceptable *horizontal homogeneity* is not achieved or if reverse flow exists. It is more time-efficient to check for numerical errors at this stage. If an acceptable agreement is achieved between the inlet and test area flow conditions, the model geometry can be created, and a grid sensitivity test can be started. Choosing the appropriate turbulence model, grid size, and near-wall

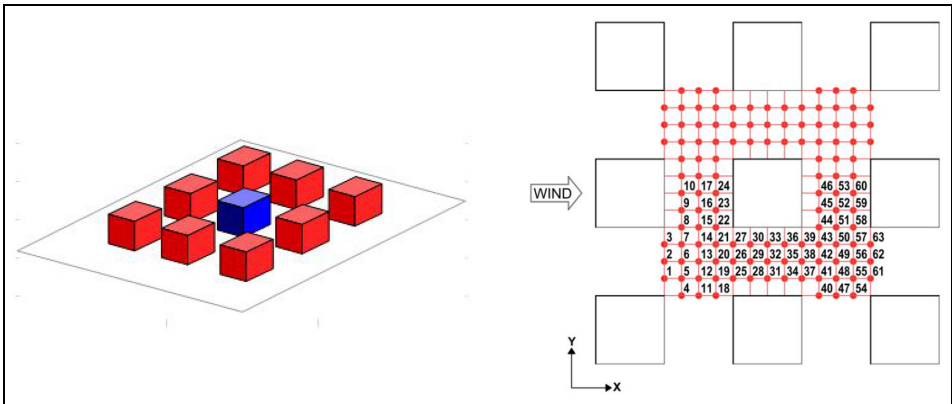


Figure 5. 3-D view of simple building blocks-Test Case C, Sub-Case 1H (left) and plan view of the measurement points around the central building (right) (AIJ, 2016).

treatment usually yields accurate results. However, if the results are not satisfactory, other turbulence models should be tested and the grid size reduced.

Experimental data. It is necessary to obtain reliable experimental datasets generated in ABL to validate an urban CFD model. The Working Group of the Architectural Institute of Japan (AIJ, 2016) provided many online wind tunnel datasets files (Excel) for CFD validation purposes and published validation benchmark tests of seven different comparative and parametric studies to assess the pedestrian wind environment around buildings in ABL. The wind tunnel datasets file provides inlet boundary conditions, measurement points for each test scenario, and detailed experimental results.

In this article, standard simple building blocks (Test Case C) proposed by the AIJ (2016) are used for CFD validation. The sub-case (Case 1H) of Test Case C (AIJ) consists of a 3×3 layout of uniform height (20 m) blocks with a 20 m street width. The central building has the same height as the surrounding buildings, and the scale ratio of the buildings is 1:1:1 (height: width: length). The sub-case (Case 1H) represents a standard city plan. Figure 5 (left) shows the sub-case (Case 1H) proposed by the AIJ.

The experimental study was carried out in an ABL wind tunnel at a reduced scale of 1/100, and all the values in the calculations were also indicated at the same scale. Wind speed was measured from the ground of the wind tunnel at 2 cm height (pedestrian level), corresponding to 2 m at full scale. The Test Case C dataset consists of 120 wind speed measurement points around the central building shown in Figure 5 (right). We assessed half of the measurement points (1–63) since the geometry of the sub-case (Case 1H) and the measurement points are symmetrical. The dataset uses mean wind speed for systematic point-to-point comparison.

During the validation process, the experimental and the CFD results of scalar wind speed were compared only for the normal wind flow direction ($\phi = 0^\circ$). Wind speed values are normalized to the reference wind speed. Expressing the wind speed as a ratio allows for easy cross-comparison of different points. The wind speed ratio formula is expressed as: $W.S.R = U/U_{ref}$

where U is the mean wind speed at the measurement point and U_{ref} is the inlet mean wind speed ($z = 2$ cm).

Size of computational domain. The computational domain should have appropriate dimensions to keep the effect of computational boundaries on wind speed as minimum as possible. In CFD validation with wind tunnel testing, the computational domain for the CFD model should have the same geometric dimensions and cross-section as the wind tunnel. Therefore, the lateral and upper size of the computational domain is limited by the wind tunnel size, 1.8 m (9H) \times 3.0 m (15H) (height \times width), where H is the height of the building. The inlet boundary edge was located at 10H, and the outflow boundary edge was located at 15H from the building (Franke et al., 2007).

Boundary conditions. For a realistic CFD solution in ABL studies, the inlet wind profile should be created using the logarithmic law corresponding to the terrain exposure category or the profile obtained from the wind tunnel experiment. For the ground surface boundary condition, it is necessary to specify the aerodynamic roughness length (z_0) (Wieringa, 1992) or the equivalent sand-grain roughness height (k_s) (Nikuradse, 1933).

Inlet boundary condition. The inlet wind velocity U (m/s) and the RMS value of velocity fluctuation σ_u (m/s) were obtained from the experimental inlet wind profile for the lower parts of the ABL (0–120 m at full scale). However, turbulence kinetic energy $k(z)$ and turbulence dissipation (ϵ) in the vertical direction is also necessary for CFD simulations in STAR-CCM + . The inlet boundary conditions for the standard k-epsilon and realizable k-epsilon models are defined with the $k(z)$ and (ϵ) turbulence specification methods in STAR-CCM + . However, unlike these two models, the Reynolds stress model solves the six Reynolds Stress components of the Reynolds stress tensor. In STAR-CCM + , the Reynolds Stress model was also specified solely in terms of $k(z)$ and (ϵ) instead of Reynolds Stress components. However, with this option, boundary turbulence conditions are assumed to be isotropic (Star-CCM + , 2006).

Using the U and σ_u values, turbulence kinetic energy $k(z)$ was calculated from the relation between $k(z)$ and $\sigma_u(z)$:

$$k(z) \cong \sigma_u^2(z) \quad (1)$$

After obtaining the $k(z)$ values for different heights, the values of turbulence dissipation (ϵ) were calculated from the relation $P_k = (\epsilon)$, (P_k : production term for k equation):

$$\varepsilon(z) \cong P_k(z) \cong C_\mu^{1/2} \cdot k(z) \cdot dU(z)/dz, \text{ where } C_\mu \text{ is the model constant } (= 0.09). \quad (2)$$

Ground surface boundary condition. Two methods can be used to model the ground surface boundary condition: aerodynamic roughness length (z_0) using the updated Davenport (1961) roughness classification (Wieringa, 1992) or the equivalent sand-grain roughness height (k_s). Since STAR-CCM+ uses roughness properties based on k_s , we calculated k_s for the CFD model. Blocken et al. (2007b) recommend using the equation (equation (3)) based on the relation of the parameters of z_0 , k_s , and c_s (roughness constant) for horizontal homogeneity in ABL flow and state that this equation can be applied to any CFD code. The equation between k_s and z_0 :

$$k_s = \frac{9.793 \cdot z_0}{C_s} \quad (3)$$

The value of z_0 was calculated using the inlet experimental data (U_{ref} at z_{ref}) and the logarithmic law:

$$\frac{U_{\text{ref}}}{(\tau_w/\rho)^{1/2}} = \frac{1}{\kappa} \ln \left(\frac{z_{\text{ref}}}{z_0} \right) \quad (4)$$

If the boundary layer formed near the ground can be regarded as the constant flux layer, the value of z_0 can be assumed from the logarithmic law using the relation $(\tau_w/\rho)^{1/2} = u^* = C_\mu^{1/4} \sqrt{k}$. The friction velocity (u^*) was estimated by the following equation using the value of turbulence kinetic energy (k) at the closest point from the ground ($z_{\text{ref}} = 1 \text{ cm}$) in the experiment.

$$u^* \cong C_\mu^{1/4} \sqrt{k} = 0.09^{1/4} \sqrt{0.314} = 0.307 \text{ m/s, where } C_\mu \text{ is the model constant } (= 0.09). \quad (5)$$

Using calculated friction velocity (u^*) and U_{ref} at the height of z_{ref} (1 cm) in equation (4), the value of z_0 was calculated to be $4.386 \times 10^{-2} \text{ cm}$. The von Karman constant (κ) is imposed in this study as 0.41. Using the obtained z_0 value from equation (4), k_s was found as 0.43 cm where the value of c_s is 1.0.

Lateral, upper, and building surface boundary conditions. The logarithmic law of no-slip shear stress and smooth wall surface feature was applied to the building surfaces. Slip/Symmetrical wall boundary condition was applied for the lateral and upper boundaries to avoid resolving the boundary layer of the wind tunnel wall. However, ignoring the frictional effects of wind tunnel boundaries can affect the simulation results. Therefore, we compared the impact of the no-slip/smooth and slip/symmetric wall boundary conditions on wind flow and found no change in the results. It means that the lateral and upper boundary condition of the wind tunnel where the AIJ TEST Case C was conducted does not affect the experiment result. This is reasonable considering the blockage ratio ($\text{Area}_{\text{buildings}}/\text{Area}_{\text{domain}}$) of 2.2% in the experiment. At the outlet boundary, open boundary conditions were used, and zero static pressure was applied.

Turbulence models. In pedestrian wind comfort studies, it is usually sufficient to obtain only mean speed values; therefore, there is no need to resolve all the details of turbulent fluctuations. Steady-state RANS (Reynolds-averaged Navier–Stokes) equations are widely implemented in pedestrian wind comfort studies to calculate the time-averaged mean speed. However, since the time-averaged process on the momentum equations neglects the details of the flow state of instantaneous fluctuations, the effects of turbulence on average flow need to be calculated (Versteeg and Malalasekera, 2007). Therefore, there is a need to use an explicit turbulence model that can compute turbulent flows with RANS equations by predicting the Reynolds stresses and scalar transport terms and closing the system of mean flow equations (Versteeg and Malalasekera, 2007).

In this article, the turbulent wind flow pattern over the urban coastal patterns was obtained by solving the 3-dimensional steady Reynolds-averaged Navier Stokes (RANS) equations with the Standard $k-\varepsilon$ (Jones and Launder, 1972), Realizable $k-\varepsilon$ (Shih et al., 1995), and Reynolds Stress Model (RSM) Chou (1945) and Rotta (1951). These turbulence models are mostly used in urban wind flow applications. Due to the shortcomings of the standard $k-\varepsilon$ model, many revised or modified $k-\varepsilon$ models and differential stress model (DSM) by Tominaga et al. (2004) and Yoshie et al. (2007) and non-linear or Reynolds-stress models (RSM) by Franke et al. (2007) are recommended to improve prediction accuracy in high-speed regions. RSM is better to predict the effect of turbulent fluctuation on the mean flow and thus can provide a better prediction of velocity gradients of mean flow (Franke et al., 2007). The performance of the turbulence models was tested under the same computational conditions (grid, boundary conditions, etc.) and the flow was considered turbulent and incompressible.

Choice of computational grid. Creating a computational grid through discretization is a critical step in CFD modeling. It is also important to confirm that the CFD result does not change with different grid structures. Therefore, a grid sensitivity study should be performed. Franke et al. (2004) suggest using at least three systematically refined grids to predict the error band of spatial discretization in grid refinement.

Generally, the more grids there are, the higher the accuracy, but the longer the calculation time. CFD requires the highest simulation accuracy but is often performed under time constraints. Therefore, global grid refinement is impractical and time-consuming. Franke et al. (2007) recommend using a local grid refinement in the area of interest instead. The refinement process is of creating a denser grid structure (meshing) in certain parts of the model to achieve more precise results in the refinement area.

Grid-independence study. It is necessary to find the optimum grid resolution to ensure the accuracy of the CFD model at an acceptable run time. Therefore, a grid independence study was performed. Three points were taken into account when determining the grid sizes:

- (1) At least 10 grids are required on one side of the building (Franke et al., 2004; Tominaga et al., 2008), and at least two or three layers of control volume should be provided at the pedestrian level (0–2 m at full scale) (Franke et al., 2004).
- (2) The distance y_P (the center point (P) of the first cell) should be larger than k_s (Blocken et al., 2007b). However, it is important to note that it is impossible to meet the requirement of $y_P > k_s$ for high terrain categories such as category IV where z_0 is 1 m at full scale.
- (3) For high Reynolds number wall treatment formulation, the dimensionless normal distance (y^+) of the first cell centroids from the wall should be at least 30 ($y^+ = 30$) (Casey and Wintergerste, 2000) and should be between 30 and 150 ($30 < y^+ < 150$) (Star-CCM+, 2006).

In this context, the maximum grid cell size of the building should be 2 cm, and the height of the first cell should be ≤ 1 cm for pedestrian-level wind assessment. Considering the relation between k_s and the first grid height, the height of the first cell should be greater than 0.86 cm (> 0.86 cm), where k_s is 0.43 cm.

For the use of the wall function, we calculated the size of the first cell (y) when the desired y^+ ($30 < y^+ < 150$) equation:

$$y = \frac{y^+ \mu}{\rho u^*} \quad (6)$$

where y is the wall distance, ρ is the density of air (kg/m^3), u^* is the friction velocity, and μ is the dynamic viscosity of air ($\text{kg/m}\cdot\text{s}$). The u^* was calculated using equation (5) and found to be 0.307 m/s. For $30 < y^+ < 150$, the wall distance was calculated as $0.14 \text{ cm} < y < 0.71 \text{ cm}$. According to this result, the first cell height should be between 0.28 cm and 1.42 cm.

Based on the requirements and calculations discussed, the height of the first cell should be in the range of 0.86–1 cm, and only a 1 cm grid cell size provides the required conditions. Therefore, it is difficult to perform a grid sensitivity test with at least three systematically refined grids in the 0.86–1 cm first cell height range. To solve the problem, Blocken et al. (2007b) recommends alleviating the requirement of $y_P > k_s$ or using a coarser grid in the upstream and downstream areas and a finer grid in the test area. However, in our preliminary tests to investigate the sensitivity of the $y_P > k_s$ requirement, we found that meeting the $y_P > k_s$ requirement gives a more accurate result in such a situation with a low terrain category. In this context, we adopted four basic strategies when determining grid cell sizes in the grid sensitivity test:

- (1) Using a coarser grid in the upstream and downstream areas and a finer grid in the test area. This strategy was applied to all grid sizes.
- (2) We fulfilled the requirement of $y_P > k_s$.

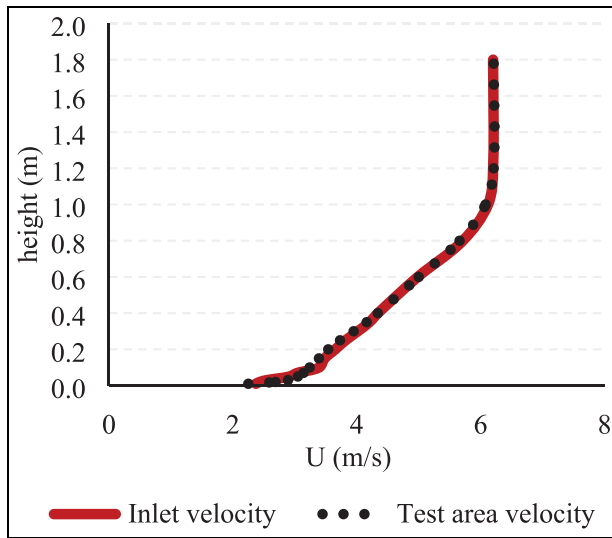


Figure 6. Vertical velocity profile comparison in an empty domain.

- (3) We alleviated the rule of providing two or three layers of control volume at pedestrian level (2 m at full scale) in the test area recommended by Franke et al. (2004) since grid cell sizes larger than 1 cm do not fulfill this rule.
- (4) We used high Reynolds number ($30 < y^+ < 150$) wall treatment method based on standard wall function.

The proper creation of the vertical velocity profile is important for high simulation accuracy. At the same time, maintaining *horizontal homogeneity* throughout the computational domain is another important point. Many studies report the difficulty in creating a horizontally homogeneous ABL flow (Blocken and Carmeliet, 2006; Franke and Frank, 2005; Zhang, 1994). It is recommended to test the velocity profile depending on the ground surface conditions in the empty computational domain (Blocken et al., 2007b; Franke et al., 2007). To check the agreement between k_s and the first cell size, the vertical velocity profile where the geometric model would first interact with the wind flow (test area) was measured in the empty computational domain. We confirmed that no large difference between the vertical velocity profile in the inlet and test area exists when the k_s is 0.43 cm and the grid cell height is 1 cm. However, the deviation in velocity is at the highest level, 5.8% in the first 5 cm (50 m at full scale) from the ground, but this difference is at an acceptable level. Figure 6 shows the vertical velocity profile comparison as a function of height.

After checking the vertical velocity profile in the test area, a grid independence study was performed in STAR-CCM + . The computational domain was divided into two different boundary areas, (the test area and the upstream and downstream

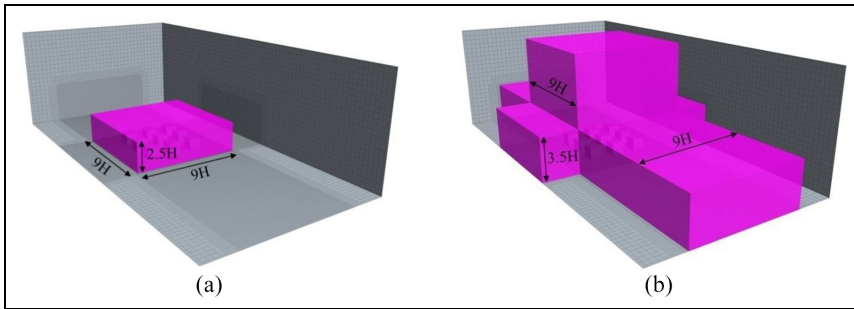


Figure 7. View of the Cartesian boxes in the computational domain (a) test area (b) upstream/downstream areas.

areas) by a set of Cartesian boxes for regional grid refinement. Figure 7(a) shows Cartesian boxes applied in the test area and Figure 7(b) in the upstream and downstream areas. The Cartesian box in the test area was kept large enough to cover the wall boundary layers, high-speed flow regions, shear layers formed by flow separation, stagnation points produced by flow impingement and wakes behind the buildings (Star-CCM + , 2006).

To reduce the computational run time, the grid is finer around the test area and coarser in the upstream and downstream areas. In the test area, we started with 20 grid cells along the building surface in each direction and gradually reduced the number of grid cells to 16 and then 10, corresponding to the absolute grid size of 1, 1.25 and 2 cm for Grid 1, Grid 2 and Grid 3, respectively. The grid cell sizes were arranged in a systematic order in the test area (12.5% of the base size), the upstream and downstream areas (25% of the base size), and the computational domain (100% of the base size). Table 1 shows the grid cell size (% of the base size), grid cell number on building surface, absolute grid cell size (cm) and the total number of cells for each test case.

For the grid shape, structured hexahedral cells were used as the buildings have a simple and regular form. In addition, 15 prism layers were applied to near-wall boundaries ($y^+ < 150$). The first prism layer has a height of 0.01 cm from the ground, and the layer size gradually increases with a stretching ratio of 1.2. While prism layers are optional, it is recommended to use 10–20 layers for high y^+ wall-function type grids to increase the accuracy further (Star-CCM + , 2006). Figure 8 shows the grid structure of the computational domain.

The grid sensitivity test was carried out with the RSM-Linear Pressure Strain turbulence model of STAR-CCM + . We used the segregated flow solver based on the SIMPLE (Semi-Implicit Method for Pressure Linked Equations) algorithm to couple the pressure and velocity equations and the second-order upwind scheme for the discretization of convection terms of the partial differential equations.

Figure 9 shows the results of the grid independence study. The results confirm that the solution is grid-independent when using grid cell size of 1.25 cm or smaller

Table 1. Grid cell size (% of the base size) in each area, grid cell number on building surface, absolute grid cell size (cm) and the total number of cells.

Grid name	Grid areas	Grid cell size (% of the base size)	Grid cell number (on building surface)	Absolute grid cell size (cm)	Total number of cell
Grid 1	Computational domain	100		8	4.837.926
	Upstream & downstream areas	25		2	
	Test area	12.5	20	1	
Grid 2	Computational domain	100		10	2.681.377
	Upstream & downstream areas	25		2.5	
	Test area	12.5	16	1.25	
Grid 3	Computational domain	100		16	735.645
	Upstream & downstream areas	25		4	
	Test area	12.5	10	2	

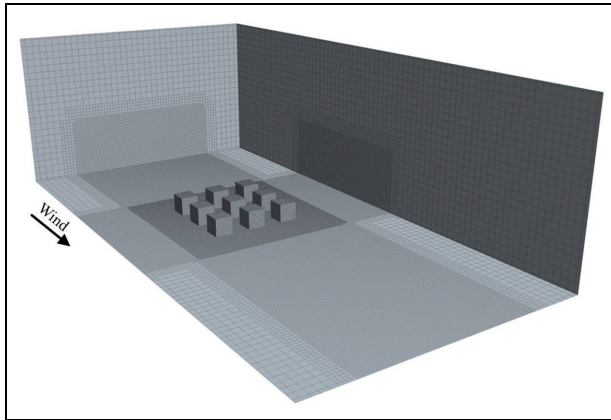


Figure 8. View of the global and local grid discretization in the computational domain.

(1 cm) as the wind speed ratio does not change with a further decrease in grid size. Grid 2 is satisfactory, that is, with one side of the building divided into 16 portions or more. However, we used a 1 cm grid cell size to provide at least two layers of control volume at the pedestrian level (2 cm). Thus we fulfilled all the requirements stated in the BPGs.

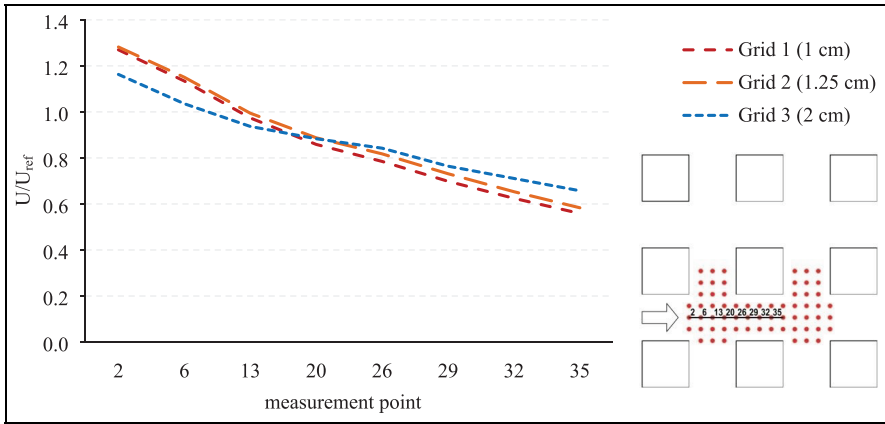


Figure 9. Comparison of the velocity profiles in the high-speed region for the three grids tested.

After the grid independence study, as another quality-control measure to reduce the spatial discretization error, we performed discretization error estimation with the Grid Convergence Method, which has been evaluated in many CFD cases (Broadhead et al., 2004; Eça et al., 2007; Roache, 1993). The GCI (grid convergence index) values for three selected grids (Grid 1, 2, and 3) at eight different measurement points (2, 6, 13, 20, 26, 29, 32, 35) on the horizontal plane ($z = 2$ cm) were calculated using the wind speed ratio (U/U_{ref}) as the critical variable (ϕ). The calculation procedure for the estimation of discretization error for the grids was explained in detail. In the first step, when $h_1 < h_2 < h_3$ where h is grid size and $r_{21} = h_2/h_1$, $r_{32} = h_3/h_2$, the apparent order p of the method was calculated using the equations (7a), (7b), and (7c) (Celik et al., 2008):

$$p = \frac{1}{\ln(r_{21})} |\ln|\varepsilon_{32}/\varepsilon_{21}| + q(p)| \quad (7a)$$

$$q(p) = \ln\left(\frac{r_{21}^p - s}{r_{32}^p - s}\right) \quad (7b)$$

$$s = 1 \cdot \text{sgn}(\varepsilon_{32}/\varepsilon_{21}), \text{ where } \varepsilon_{32} = \phi_3 - \phi_2, \varepsilon_{21} = \phi_2 - \phi_1. \quad (7c)$$

In the second step, the extrapolated values were obtained using equation (8) (Celik et al., 2008):

$$\phi_{\text{ext}}^{21} = (r_{21}^p \phi_1 - \phi_2) / (r_{21}^p - 1) \quad (8)$$

The approximate relative error using equation (9), the extrapolated relative error using equation (10), and the fine-grid convergence index using equation (11) were calculated (Celik et al., 2008). Hence, the numerical uncertainty in the fine-grid

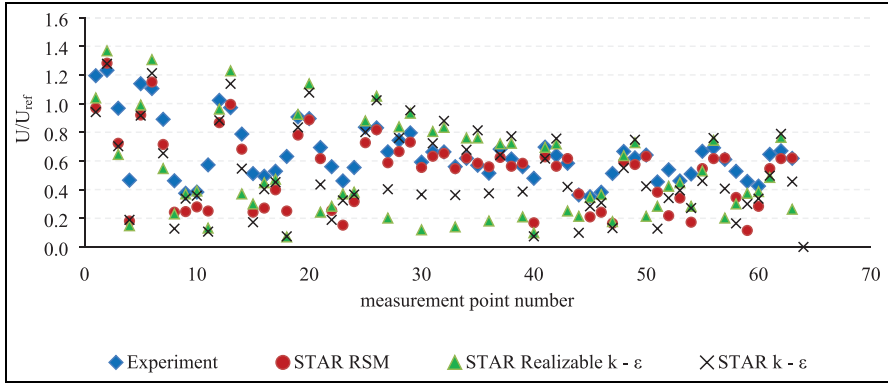


Figure 10. Comparison of wind speed ratios between experiment and different CFD turbulence models.

solution for the wind speed ratios (U/U_{ref}) was found as 0.04%, 0.5%, 0.4%, 1.6%, 3.1%, 1.8%, 10%, and 3.8% at measurement points of 2, 6, 13, 20, 26, 29, 32, and 35, respectively.

$$e_a^{21} = \left| \frac{\phi_1 - \phi_2}{\phi_1} \right| \quad (9)$$

$$e_{ext}^{21} = \left| \frac{\phi_{ext}^{12} - \phi_1}{\phi_{ext}^{12}} \right| \quad (10)$$

$$GCI_{fine}^{21} = \frac{1.25e_a^{21}}{r_{21}^p - 1} \quad (11)$$

Results of CFD validation. We evaluated the predictive accuracy of the Standard $k-\epsilon$, Realizable $k-\epsilon$, and RSM turbulence models by comparing the calculated wind speed magnitudes with the experimental results. Figure 10 shows a comparison of simulated and experimental wind speed ratios (U/U_{ref}) at 2 cm above the ground obtained with different turbulence models. The results show that there is no complete consistency with the experimental data however the position of the highest speed zone has been simulated very well by STAR-CCM+. The predictive accuracy in the high-speed region of $U/U_{ref} > 1.0$ is satisfactory for all turbulence models. High predictive accuracy in the high-speed region is important for accurately predicting high-speed wind flow and pedestrian wind discomfort risk in urban wind flow analysis.

The degree of accuracy varies considerably in the high and low-speed regions. The wind speed ratios vary greatly, especially in the Realizable $k-\epsilon$ and the Standard $k-\epsilon$ models. The general trend is that CFD prediction has limited accuracy in wind-sheltered areas behind buildings. In these regions, the wind speed ratio was underestimated and found lower than in the experiment. Turbulence

Table 2. The percent error for each CFD code and turbulence model.

CFD Code	Turbulence model	Percent error (%) where $U/U_{ref} > 1.0$	Percent error (%) where $U/U_{ref} > 0.6$	Percent error (%) where $U/U_{ref} > 0$
STAR-CCM+	RSM	12	10.8	22.3
	Realizable $k-\epsilon$	12.2	26.5	30.7
	Standard $k-\epsilon$	13.2	21.4	30.8

models are insufficient to resolve wind-sheltered regions and are not good enough to predict low-speed regions.

Among the turbulence models, the predictive accuracy of the RSM model is remarkable and the trend of wind speed ratio is more similar to the experimental result. The position of the highest speed has been simulated very well by the RSM although it underestimates the low-speed region. There is a high deviation in wind speed ratio particularly at the measurement points 22–24 and 58–60.

To quantitatively evaluate the predictive accuracy of turbulence models, we calculated the percent error between the CFD and the experimental result using the following equation: Percent error = $|(P(v) - M(v)) / M(v)| * 100\%$

where $P(v)$ is the predicted wind velocity calculated by CFD and $M(v)$ is the measured wind velocity obtained from the wind tunnel experiment. Table 2 shows the percent error for each turbulence model. The table shows that there is moderate agreement in the low-speed regions and a higher level of agreement in the high-speed regions. The percent error increases for each turbulence model where in the regions the wind speed ratio decreases.

CFD validation results showed that the predictive accuracy of RSM is better than other turbulence models, with a percent error of around 22.3%. This high percent error is mainly due to the low predictive accuracy in the side-street flow region. However, the most important point in wind comfort assessment is to find the highest speed region and position with acceptable accuracy. The percent error of RSM is around 12% in the high-speed region where $U/U_{ref} > 1.0$. In addition, it is 10.8, 17.3 and 21.3% where $U/U_{ref} > 0.6, 0.5$ and 0.4 , respectively. The RSM provides higher predictive accuracy in the flow region where $U/U_{ref} > 0.6$. In the evaluation of the high-speed regions with steady RANS, a percent error of up to 10% is considered “very good,” while 20% is considered “good” (Blocken et al., 2016). In addition, a percent error of up to 25% can be accepted in urban aerodynamic studies with steady RANS models.

The Realizable $k-\epsilon$ and Standard $k-\epsilon$ models show medium predictive accuracy. The percent error is 30.7% and 30.8%, respectively where $U/U_{ref} > 0$. However, these turbulence models could be used to predict the high wind speed ratios where $U/U_{ref} > 1.0$ with acceptable accuracy in pedestrian wind comfort studies.

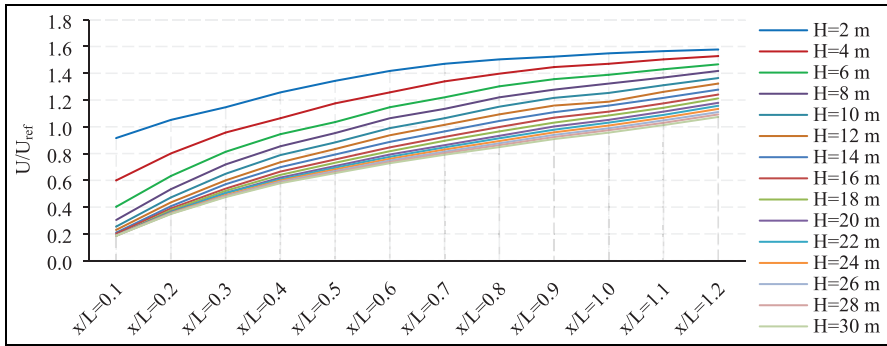


Figure 11. Maximum wind speed ratios (U/U_{ref}) in the horizontal plane ($z = 2$ m at full scale) on PCA.

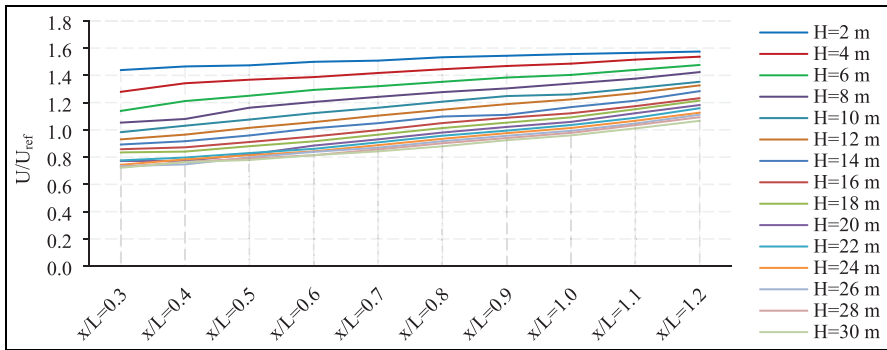


Figure 12. Maximum wind speed ratios (U/U_{ref}) in the horizontal plane ($z = 2$ m at full scale) on UBC.

CFD setup to simulate urban coastal patterns. In CFD tests of all urban coastal patterns, we used the same boundary conditions, grid size, and numerical scheme specified in the CFD validation process, and RSM as it is more consistent with the experimental results. Since a large number of test cases (195) were simulated in this study, the simulations were performed at a reduced scale (1/100), the same as the wind tunnel scale, to conserve numerical resources without neglecting the predictive accuracy (Ai and Mak, 2014). The blockage ratio was kept below 3%, and wind speed was measured at 2 cm height.

Results

Effect of x/L ratio and H on wind speed conditions

The standard and proposed urban coastal patterns were simulated, and the maximum wind speed ratios (U/U_{ref}) were calculated on PCA, CBC, and UBC. We

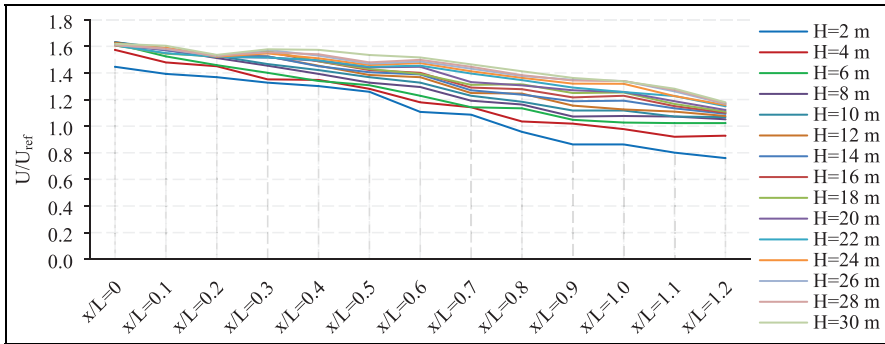


Figure 13. Maximum wind speed ratios (U/U_{ref}) in the horizontal plane ($z = 2$ m at full scale) on CBC.

found two correlations: the first is between the x/L ratio and U/U_{ref} , and the second is between the central building height (H) and U/U_{ref} . In general, the lower the x/L ratio and the higher the central building height (H), the lower the risk of wind discomfort on PCA (Figure 11) and UBC (Figure 12). Parametrically, as the x/L ratio increases, U/U_{ref} gradually increases, on the contrary, as H increases, U/U_{ref} decreases on PCA and UBC. Maximum wind speed ratios (U/U_{ref}) range from 0.18 and 1.57 on PCA and from 0.72 to 1.57 on UBC depending on the x/L ratio and H . The lowest U/U_{ref} (0.18) on PCA is provided by the urban coastal pattern with an x/L ratio of 0.1 and H of 30 m, while the highest U/U_{ref} (1.57) is provided by the urban coastal pattern with an x/L ratio of 1.2 and H of 2 m.

Unlike PCA and UBC, the correlation between the x/L ratio and U/U_{ref} and H and U/U_{ref} are inverse on CBC. In general, reducing the x/L ratios and increasing H increases the wind discomfort risk on CBC (Figure 13). Parametrically, as the x/L ratio increases, U/U_{ref} decreases, on the contrary, as H increases, U/U_{ref} increases on CBC. The lowest U/U_{ref} (0.76) is provided by the urban coastal pattern with an x/L ratio of 1.2 and H of 2 m, while the highest U/U_{ref} (1.57) is provided by the urban coastal pattern with an x/L ratio of 0 and H of 30 m.

The ultimate aim of the wind assessment is to determine the optimum x/L ratios for each central building height (H) and the *best possible urban coastal pattern* within all simulated patterns providing minimum wind discomfort risk on PCA, UBC, and CBC. However, the results of the simulations are conflicting: the lower x/L ratio with higher H cause minimum wind discomfort risk on PCA and UBC, while the higher x/L ratio with lower H , causes minimum wind discomfort risk on CBC. Since the maximum wind speed ratios vary on PCA, UBC, and CBC, we optimized the results and determined the optimum x/L ratios with a cross-comparison of the wind speed ratios on PCA, UBC and CBC. Figure 14 shows the optimum x/L ratios for each central building height. It is noteworthy that optimum x/L ratios generally correspond to the intersections of the PCA and CBC

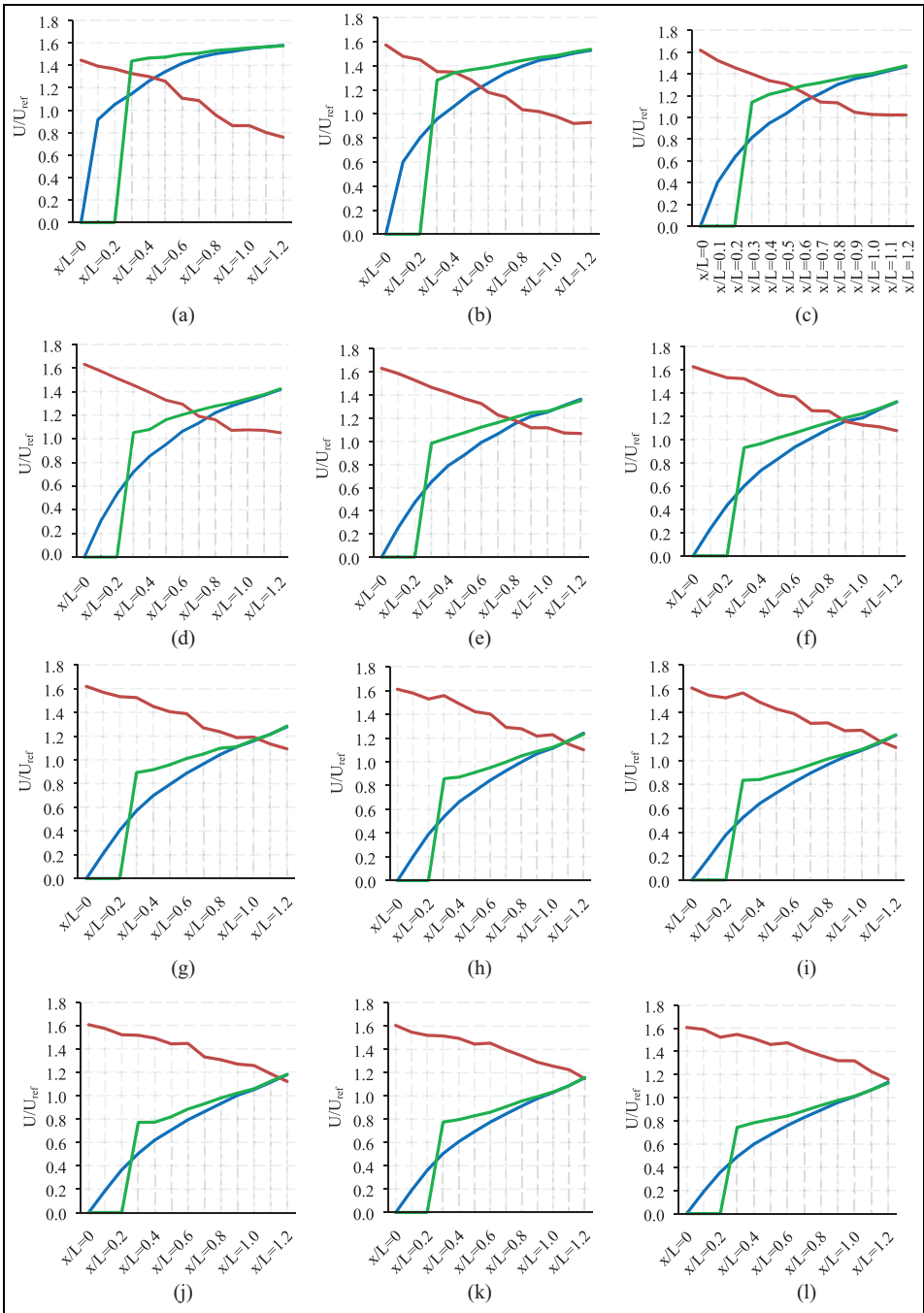


Figure 14. Continued

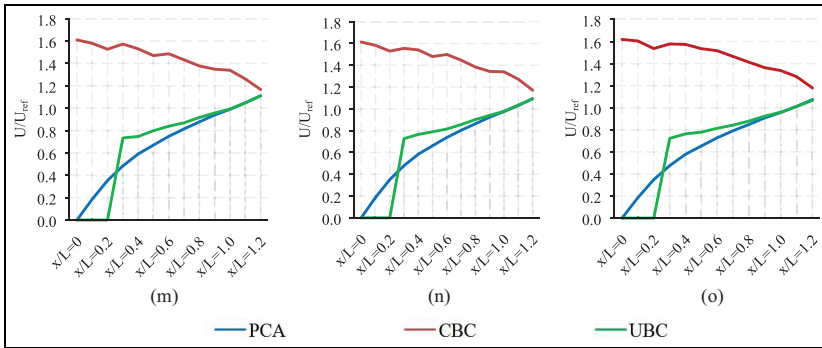


Figure 14. Maximum wind speed ratios (U/U_{ref}) in the horizontal plane ($z = 2$ m at full scale) on PCA, CBC, and UBC: (a) $H = 2$ m, (b) $H = 4$ m, (c) $H = 6$ m, (d) $H = 8$ m, (e) $H = 10$ m, (f) $H = 12$ m, (g) $H = 14$ m, (h) $H = 16$ m, (i) $H = 18$ m, (j) $H = 20$ m, (k) $H = 22$ m, (l) $H = 24$ m, (m) $H = 26$ m, (n) $H = 28$ m and (o) $H = 30$ m.

Table 3. Integrated performance index of maximum wind speed ratios (U/U_{ref}) as a function of H coupled with the optimum x/L ratios.

H (m)	2	4	6	8	10	12	14	16	18	20	22	24	26	28	30
x/L ratio	0.4	0.5	0.6	0.7	0.8	0.9	0.9	1.1	1.1	1.2	1.2	1.2	1.2	1.2	1.2
PCA	1.25	1.17	1.14	1.13	1.15	1.15	1.11	1.17	1.14	1.18	1.16	1.13	1.11	1.09	1.07
CBC	1.30	1.28	1.22	1.19	1.18	1.15	1.18	1.15	1.16	1.12	1.14	1.15	1.17	1.17	1.18
UBC	1.46	1.36	1.29	1.24	1.20	1.18	1.11	1.17	1.15	1.18	1.16	1.12	1.11	1.09	1.07
	(best possible)														
U/U_{ref}	1.00–1.10			1.11–1.15			1.16–1.20			1.21–1.25			1.26–1.50		

lines. However, in general, the intersections of the PCA and CBC lines do not coincide with the x/L ratios tested. Therefore, we determined the urban coastal patterns closest to the optimum x/L ratios. When the H is 2, 4, 6, 8, 10, 12, 14, 16, and 18 m, optimum x/L ratios were found as 0.4, 0.5, 0.6, 0.7, 0.8, 0.9, 0.9, and 1.1, respectively and when the H is more than 18 m, optimum x/L ratio was found as 1.2. These 15 urban coastal patterns cause a minimum risk of wind discomfort compared to other simulated patterns at each central building height.

The results highlight that proper matching of the x/L ratio and H at the intersection points can reduce the risk of wind discomfort on PCA, UBC and CBC. In general, lower H performs well with a lower x/L ratio, while higher H performs well with a higher x/L ratio. Therefore, if the height of the central building (H) is increased, the x/L ratio should also be increased proportionally to minimize the risk of wind discomfort.

After determining the optimum x/L ratios for each central building height, an integrated performance index was created to determine the *best possible urban coastal pattern* as a function of H and the optimum x/L ratios of 15 optimum urban coastal patterns. Table 3 shows how to assess overall wind discomfort risk on PCA, UBC, and CBC based on the maximum wind speed ratio (U/U_{ref}). To assess the wind discomfort risk, U/U_{ref} values between 1.00 and 1.50 were divided into five zones, 1.0–1.10, 1.11–1.15, 1.16–1.20, 1.21–1.25, and 1.26–1.50 which represent five different highlights from lightest to darkest. The lightest highlight corresponds to the U/U_{ref} between 1.0 and 1.10 and provides minimum wind discomfort risk, while the darkest highlight corresponds to the U/U_{ref} between 1.26 and 1.50 and yields maximum wind discomfort risk.

According to Table 3, a noteworthy finding is that the pattern with an x/L ratio of 1.2 and H of 24m appears to be the best since it provides the optimized wind conditions with a maximum U/U_{ref} of no more than 1.13 on PCA and UBC and 1.15 on CBC. While this pattern has been determined to be the *best possible urban coastal pattern*, it does not mean that designers are only required to use it, as other urban coastal patterns with H values between 10 and 30 m result in only 2% to 5% higher wind speed ratios. This result is desired by designers as it provides flexibility and the largest selection framework in creating design options. Thus, designers can apply a wide range of urban coastal patterns combining different x/L and H depending on their other specific architectural needs and concerns.

The relatively highest central building ($H = 30$ m) with an x/L ratio of 1.2 was eliminated since it outperforms the best possible urban coastal pattern on PCA and UBC (6%) but is worse than it on CBC (3%). Increasing H much more can result in more wind discomfort risk as there is a positive correlation between increased H and wind speed on CBC. Similar to our findings, increased wind flow acceleration at the corner of buildings with increasing building height has been extensively reported in previous studies (Reiter, 2010; Stathopoulos and Blocken, 2016).

Depending on the urban function and pedestrian activity to be assigned to the PCA, UBC, and CBC during the design process, some areas may be more critical than others in terms of wind discomfort risk, and designers may determine the best possible urban coastal pattern based on this particular situation. For example, if only UBC (pedestrian sidewalk) is the critical location for pedestrian wind comfort in a design, the best possible urban coastal pattern is the one that performs best in UBC. However, this article gives equal priority to wind conditions in PCA, UBC, and CBC because, in most cities, the coastal passages are generally pedestrianized and used entirely by pedestrians. Therefore, we optimized the results taking into account PCA, UBC, and CBC equally, and determined the best possible urban coastal pattern based on the argument that the pattern provides a minimal risk of wind discomfort in the entire evaluation region.

Figure 15 shows contour plots of wind speed ratios of three urban coastal patterns. In the standard urban coastal pattern, the *double corner effect* on PCA is dominant with a U/U_{ref} of 1.60 (Figure 15(a)). Yet, the *double corner effect* on PCA significantly reduced in the best possible urban coastal pattern (Figure 15(c)). The

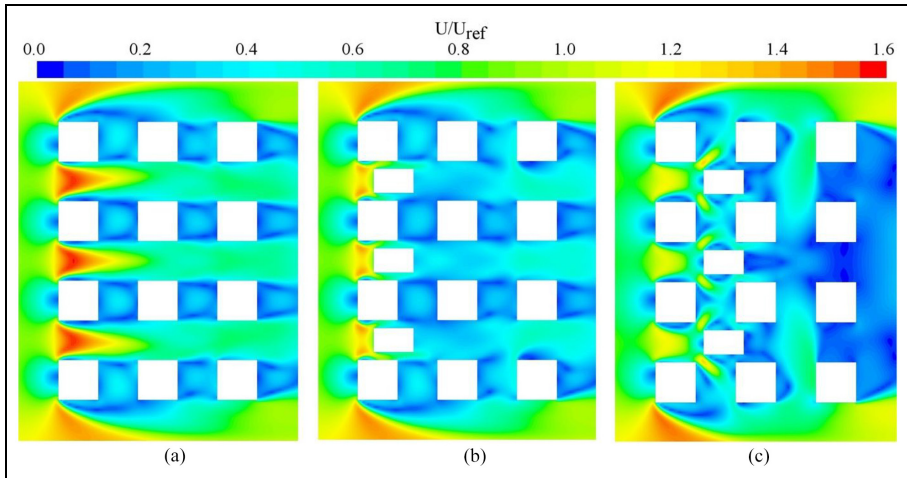


Figure 15. Contour plots of wind speed ratios of three urban coastal patterns ($z = 2$ m at full scale) (a) the standard urban coastal pattern, (b) the minimum-height urban coastal pattern ($x/L = 0.4$, $H = 2$ m), and (c) the best possible urban coastal pattern ($x/L = 1.2$, $H = 24$ m).

maximum U/U_{ref} on PCA (1.15) is 45% lower than the maximum U/U_{ref} of the standard urban pattern (1.60); this indicates that the wind climate has improved by almost 45% in the coastal passage. Figure 15(b) shows that the lowest central building ($H = 2$ m) with an x/L ratio of 0.4 yields significantly more U/U_{ref} on PCA (1.26), UBC (1.46), and CBC (1.30) than the best possible urban coastal pattern. The *corner effect* on UBC is more dominant than the *corner effect* on CBC and the *double corner effect* on PCA. When H is low (2 m), even the best possible x/L ratio (0.4) for that height is used, U/U_{ref} is significantly higher than the best possible urban coastal pattern but lower than the standard urban coastal pattern.

Effect of central building width and length on wind speed conditions

The central building width (W) and length (L) were kept at 12 and 20 m in all simulations. In addition, we performed simulations using the best possible urban coastal pattern to understand the effect of different widths (8 and 10 m) and lengths (10 and 30 m) of the central building on wind speed conditions.

The effect of central building width on wind speed ratio (U/U_{ref}) is shown in Figure 16(a). The larger building width (12 m) provides lower U/U_{ref} on PCA, UBC, and CBC than the lower building widths of 8 and 10 m. It is clear that the central building width, like the building height, is an effective parameter in reducing the risk of wind discomfort. Figure 16(b) shows the effect of central building length on wind speed ratio (U/U_{ref}). The longer building lengths (20 and 30 m) yield lower U/U_{ref} on PCA, UBC, and CBC than the shorter building lengths of 10 m. Unlike

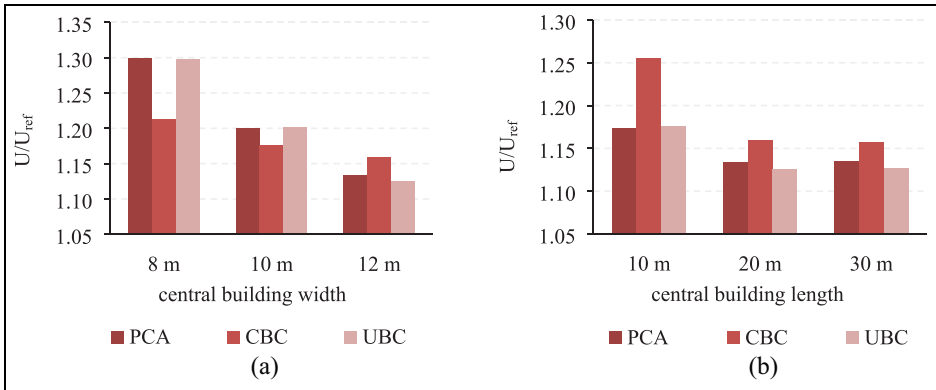


Figure 16. Maximum wind speed ratios (U/U_{ref}) in the horizontal plane ($z = 2$ m at full scale) on PCA, UBC and CBC, depending on the central building width (a), and the central building length (b).

the central building width, the central building length is more effective in reducing the risk of wind discomfort on CBC. Findings on central building length are consistent with many previous studies. A building form with a maximum L/H (length/height) provides less aerodynamic resistance to the wind flow (Beranek and Van Koten, 1979), and therefore yield less wind flow acceleration at its corners. In addition, the building length supports the reconnection of the flow, and the flow rapidly turns toward the track (Bottema, 1993). Additional simulations on the best possible urban coastal pattern showed that pre-determined dimensions of the central building ($W = 12$ m and $L = 20$ m) performed well in reducing wind discomfort risk.

Discussion

Evaluation of the results

Given that coastal buildings are exposed to open wind conditions, the *corner effect* developing around buildings and the *double corner effect* at coastal passages are inevitable. Many studies have focused on reducing the intensity of the *corner effect* (Bottema, 1993) and the *double corner effect* (Bas et al., 2022) that occurs around the buildings. In general, reducing the building height (Reiter, 2010; Stathopoulos and Blocken, 2016), using rounded-circular building corners (Bottema, 1993; Mittal et al., 2019), and shifting building configuration (Bas et al., 2022) are beneficial in improving pedestrian wind comfort. Despite similarities with previous studies aimed at reducing the risk of wind discomfort by using similar building geometries, this study presented a new design strategy that addresses the combined use of two critical variables, location (x/L) and height (H) of a central building. The best possible urban coastal pattern in this study performed relatively well, with a wind speed reduction of about 45% compared to many studies suggesting a round-circular building corner with a 30% reduction (Bottema, 1993; Xu et al., 2017) and a shifted building configuration with a 60% reduction (Bas et al., 2022).

This study also differs in that it supports a flexible design process. Although the best possible urban coastal pattern was proposed in this article, this does not mean that the designers will apply it alone, because the wind speed ratio of other urban coastal patterns between 10 and 30 m high is only 2 to 5% higher. In light of these comparative findings, the results provide designers with a broad selection framework from which they can apply a wide variety of urban coastal patterns combining different x/L and H depending on other specific architectural needs and concerns in the design process.

Based on the above discussion, this study makes a theoretical scientific contribution to the existing literature on improving the ability of coastal cities to adapt to strong wind conditions. The practical implications of this study could be enormous for communities and residents. Improving pedestrian wind comfort in urban open spaces will also support pedestrian activity, urban walkability and cycling, the livability of urban environments, and high-quality urban living. These implications can affect people's lifestyles and help make coastal cities more comfortable and livable. The results of this study can also encourage architects and city planners to design wind-comfortable urban areas for pedestrians and contribute to the development of urban planning policies regarding pedestrian wind comfort.

Limitations

In this study, the emphasis is on pedestrian wind comfort in coastal cities under the influence of sea breeze. Although urban ventilation by sea breeze is beyond the scope of this study, discussion of urban ventilation may also be useful for future studies, as sea breeze also provides benefits for reducing the urban heat island (UHI) effect through ventilation. Coastal cities in the Northern and Southern climate zones have different climatic conditions, which may require a different hierarchy of design priorities regarding urban wind flow. In northern coastal cities, pedestrian wind comfort is an important priority due to strong wind conditions (Johansson and Yahia, 2020; Szűcs, 2013), while in tropical and subtropical climates, urban ventilation is given priority to provide heat dissipation with gentle sea breezes (Ng, 2009). Although this study is hypothetical and not specific to a climate, the outcomes of this study are more suitable for the windiest coastal cities such as Wellington (NZ), St. John's (CAN), and Copenhagen (DEN), where the average wind speed is around 6.6, 6.2, and 5.6 m/s, respectively (USDOE EnergyPlus, 2021).

The front line of the coastal urban fabric is where the wind flow accelerates the most and is drawn into the city. Adding a new central building between parallel buildings increases the density and compactness of the coastal urban pattern. Many coastal cities are in dense form or in the process of densification, avoiding *urban sprawl* in the context of sustainable urbanization. Therefore, the design approach adopted in this study supports today's compact and dense sustainable city approach. However, the best possible urban coastal pattern designed based on the densification strategy can reduce downstream ventilation in the inner city even though it significantly reduces the accelerating wind speed on the coastal passage and ventilates the wind-shielded area behind the upwind buildings by diverting the

wind flow to the side streets. Depending on climatic needs and priorities, if both ventilation and pedestrian wind comfort are prioritized in a coastal city, downstream ventilation in an inner city can be improved in many ways such as by keeping the streets wide (Hussain and Lee, 1980; Kubilay et al., 2017) or adding a few relatively taller buildings to critical locations that divert free-stream wind from higher altitude to pedestrian level (Ng, 2009; Rajagopalan et al., 2014).

Future perspectives

This article focuses only on the design of the urban coastal patterns adapted to strong wind conditions without considering the effect of wind on the cooling and ventilation of urban open spaces. Future research will focus on developing an urban coastal model that considers the comfort, cooling and ventilation aspects of the wind.

Conclusion

This article presented the effect of modifying a standard urban coastal pattern on wind climate in coastal passages by strategically placing a new central building between two parallel upwind buildings. We tested the effect of critical variables, the central building's location (x/L ratio) and dimensions (*height, width, length*) on wind speed conditions with a parametric design approach based on CFD simulations.

The main conclusion is that an optimum combination and joint contribution of the two critical variables, x/L ratio and H , has a profound impact on wind speed conditions and can significantly reduce the risk of wind discomfort on the passage center axis (PCA), upwind building corners (UBC) and central building corners (CBC). In general, a lower H performs well with a lower x/L ratio, while a higher H performs well with a higher x/L ratio. When H is 2, 4, 6, 8, 10, 12, 14, 16, and 18 m, the best possible x/L ratios are 0.4, 0.5, 0.6, 0.7, 0.8, 0.9, 0.9, 1.1, and 1.1, respectively and when H is more than 18 m, the best possible x/L ratio is 1.2. The best possible urban coastal pattern with an x/L ratio of 1.2 and H of 24 m significantly minimizes *corner* and *double corner effect* with a minimum U/U_{ref} of 1.15 on CBC, 1.13 on PCA and 1.12 on UBC. The wind climate has improved by almost 45% in the coastal passage of this pattern than the standard urban pattern. The findings apply to newly-designed coastal settlements where wind shelter is required and can help urban policymakers and designers in improving pedestrian-level wind conditions in coastal urban environments.

Acknowledgements

The authors thank the anonymous reviewers for their valuable comments and suggestions that improve the article.


Declaration of conflicting interests

The author(s) declared no potential conflicts of interest with respect to the research, authorship, and/or publication of this article.

Funding

The author(s) disclosed receipt of the following financial support for the research, authorship, and/or publication of this article: This work was financially supported by the Local Environment Management and Analysis (LEMA) Unit of the University of Liège.

ORCID iD

Hakan Baş  <https://orcid.org/0000-0002-3316-9860>

References

- Ai ZT and Mak CM (2014) Potential use of reduced-scale models in CFD simulations to save numerical resources: Theoretical analysis and case study of flow around an isolated building. *Journal of Wind Engineering and Industrial Aerodynamics* 134: 25–29.
- Architectural Institute of Japan (2016) *AIJ Benchmarks for Validation of CFD Simulations Applied to Pedestrian Wind Environment Around Buildings*. Tokyo: Architectural Institute of Japan.
- Bas H, Dogrusoy IT and Reiter S (2022) Wind adaptive urban seafront buildings design for improving urban ventilation and pedestrian wind comfort in Mediterranean climate. *International Journal of Global Warming* 28(3): 239–259.
- Beranek WJ and Van Koten H (1982) *Beperken van Windhinder Om Gebouwen*. Deventer: Stichting Bouwresearch Kluwer Technische Boeken BV.
- Beranek WV and Van Koten H (1979) *Beperken van Windhinder Om Gebouwen, Deel 1*. Deventer: Stichting Bouwresearch.
- Blocken B, Carmeliet J and Stathopoulos T (2007a) CFD evaluation of wind speed conditions in passages between parallel buildings—effect of wall-function roughness modifications for the atmospheric boundary layer flow. *Journal of Wind Engineering and Industrial Aerodynamics* 95(9-11): 941–962.
- Blocken B, Stathopoulos T and Carmeliet J (2007b) CFD simulation of the atmospheric boundary layer: Wall function problems. *Atmospheric Environment* 41(2): 238–252.
- Blocken B and Carmeliet J (2006) The influence of the wind-blocking effect by a building on its wind-driven rain exposure. *Journal of Wind Engineering and Industrial Aerodynamics* 94(2): 101–127.
- Blocken B, Stathopoulos T, Carmeliet J, et al. (2011) Application of computational fluid dynamics in building performance simulation for the outdoor environment: An overview. *Journal of Building Performance Simulation* 4(2): 157–184.
- Blocken B, Stathopoulos T and van Beeck JPAJ (2016) Pedestrian-level wind conditions around buildings: Review of wind-tunnel and CFD techniques and their accuracy for wind comfort assessment. *Building and Environment* 100: 50–81.
- Bottenga M (1993) *Wind Climate and Urban Geometry*. Eindhoven: Technische Universiteit Eindhoven.
- Broadhead BL, Rearden BT, Hopper CM, et al. (2004) Sensitivity- and uncertainty-based criticality safety validation techniques. *Nuclear Science and Engineering* 146: 340–366.
- Casey M and Wintergerste T (2000) *ERCOFTAC Best Practice Guidelines for Industrial CFD*. Brussels: ERCOFTAC. (available online via <https://www.ercoftac.org>).
- Casey M and Wintergerste T (2000) ERCOFTAC Special Interest Group on quality and trust in industrial CFD. In: *Best Practice Guidelines, European Research Community on Flow, Turbulence and Combustion*. pp.123–148.

- Celik IB, Ghia U, Roache PJ, et al. (2008) Procedure for estimation and reporting of uncertainty due to discretization in CFD applications. *Journal of Fluids Engineering* 130(7): 078001.
- Chen G, Rong L and Zhang G (2021) Impacts of urban geometry on outdoor ventilation within idealized building arrays under unsteady diurnal cycles in summer. *Building and Environment* 206: 108344.
- Chou PY (1945) On velocity correlations and the solutions of the equations of turbulent fluctuation. *Quarterly of Applied Mathematics* 3(1): 38–54.
- City of London and RWDI (2019) *Wind Microclimate Guidelines for Developments in the City of London*. London: City of London Corporation.
- Davenport AG (1961) The application of statistical concepts to the wind loading of structures. *Proceedings of the Institution of Civil Engineers* 19(4): 449–472.
- DeKay M and Brown GZ (2013) *Sun, Wind, and Light: Architectural Design Strategies*. Hoboken: John Wiley & Sons.
- Dürr J, Geissler A and Hoffmann C (2023) Development of a multi-criteria decision-making model to assist building designers in the choice of superficial construction systems in urban areas. *Journal of Building Physics* 46(5): 513–540.
- Eça L, Hoekstra M and Roache PJ (2007) Verification of calculations: An overview of the 2nd Lisbon Workshop, Second Workshop on CFD Uncertainty Analysis. In: *AIAA Computational Fluid Dynamics Conference*, Miami, FL, June, AIAA Paper No. 2007-4089.
- Franke J and Frank W (2005) Numerical simulation of the flow across an asymmetric street intersection. In: *Proceedings of the Fourth European and African Conference on Wind Engineering*, pp.116–117.
- Franke J, Hellsten A, Schlünzen H, et al. (2007) *Best Practice Guideline for the CFD Simulation of Flows in the Urban Environment*. COST Action 732. *Quality Assurance and Improvement of Meteorological Models*. Hamburg: University of Hamburg, Meteorological Institute, Center of Marine and Atmospheric Sciences.
- Franke J, Hirsch C, Jensen AG, et al. (2004) Recommendations on the use of CFD in wind engineering. In: *Proceedings of the International Conference on Urban Wind Engineering and Building Aerodynamics* (ed. van Beeck JPAJ), COST Action C14, Impact of Wind and Storm on City Life Built Environment. von Karman Institute, Sint-Genesius-Rode, Belgium, 5–7 May 2004.
- Gandemer J (1978) *Discomfort due to Wind Near Buildings: Aerodynamic Concepts*, vol. 13. Washington, DC: Department of Commerce, National Bureau of Standards.
- Hussain M and Lee BE (1980) *An Investigation of Wind Forces on Three Dimensional Roughness Elements in Simulated Atmospheric Boundary Layer Flow*. Department of Building Science, University of Sheffield Report, Sheffield.
- Johansson E and Yahia MW (2020) Wind comfort and solar access in a coastal development in Malmö, Sweden. *Urban Climate* 33: 100645.
- Jones WP and Launder BE (1972) The prediction of laminarization with a two-equation model of turbulence. *International Journal of Heat and Mass Transfer* 15(2): 301–314.
- Kubilay A, Neophytou MKA, Matsentides S, et al. (2017) The pollutant removal capacity of urban street canyons as quantified by the pollutant exchange velocity. *Urban Climate* 21: 136–153.
- Lim J and Ooka R (2021) A CFD-Based optimization of building configuration for urban ventilation potential. *Energies* 14(5): 1447.

- Melbourne WH and Joubert PN (1971) Problems of wind flow at the base of tall buildings. In: *Proc. 3rd International conference on wind effects on buildings and structures*, Tokyo.
- Mittal H, Sharma A and Gairola A (2019) Numerical simulation of pedestrian level wind flow around buildings: Effect of corner modification and orientation. *Journal of Building Engineering* 22: 314–326.
- Ng E (2009) Policies and technical guidelines for urban planning of high-density cities - air ventilation assessment (AVA) of Hong Kong. *Building and Environment* 44(7): 1478–1488.
- Nikuradse J (1933) *Sturmungsgesetze in Rauhen Rohren. Forschungsheft Auf Dem Gebiete Des Ingenieurwesens*. Berlin: VDI-Verlag.
- Oke TR (1988) Street design and urban canopy layer climate. *Energy and Buildings* 11(1-3): 103–113.
- Rajagopalan P, Lim KC and Jamei E (2014) Urban heat island and wind flow characteristics of a tropical city. *Solar Energy* 107: 159–170.
- Reiter S (2010) Assessing wind comfort in urban planning. *Environment and Planning B Planning and Design* 37(5): 857–873.
- Roache PJ (1993) A method for uniform reporting of grid refinement studies. In: *Proceedings of quantification of uncertainty in computation fluid dynamics* (ed. Celik et al.), ASME Fluids Engineering Division Spring Meeting, Washington, DC, 23–24 June, ASME Publ. No. FED-Vol. 158.
- Rotta J (1951) Statistische theorie nichthomogener turbulenz. *Zeitschrift für Physik A* 129(6): 547–572.
- Shih TH, Liou WW, Shabbir A, et al. (1995) A new k- ϵ eddy viscosity model for high Reynolds number turbulent flows. *Computers & Fluids* 24(3): 227–238.
- Star-CCM+ (2006) *Star-CCM+ Version 4.02.011 User Guide*. New York: CD-adapco.
- Stathopoulos T (1985) Wind environmental conditions around tall buildings with chamfered corners. *Journal of Wind Engineering and Industrial Aerodynamics* 21(1): 71–87.
- Stathopoulos T and Blocken B (2016) Pedestrian wind environment around tall buildings. In: Tamura Y and Yoshie R (eds) *Advanced Environmental Wind Engineering*. Tokyo: Springer. pp.101–127.
- Stemmers K, Baker N, Crowther D, et al. (1997) City texture and microclimate. *Urban Design Studies* 3: 25–50.
- Szűcs (2013) Wind comfort in a public urban space—Case study within Dublin Docklands. *Frontiers of Architectural Research* 2(1): 50–66.
- Thébaud S and Millet JR (2017) Cost-effective air flow rate estimations using blowerdoor and wind speed measurements to assess building envelope thermal performances. *Journal of Building Physics* 40(6): 504–529.
- Tominaga Y, Mochida A, Shirasawa T, et al. (2004) Cross comparisons of CFD results of wind environment at pedestrian level around a high-rise building and within a building complex. *Journal of Asian Architecture and Building Engineering* 3(1): 63–70.
- Tominaga Y, Mochida A, Yoshie R, et al. (2008) AIJ guidelines for practical applications of CFD to pedestrian wind environment around buildings. *Journal of Wind Engineering and Industrial Aerodynamics* 96(10-11): 1749–1761.
- USDOE EnergyPlus (2021) Weather Data. Available at: <https://energyplus.net/weather>. (accessed 10 July 2021).
- van Hooff T and Blocken B (2010) Coupled urban wind flow and indoor natural ventilation modelling on a high-resolution grid: A case study for the Amsterdam Arena stadium. *Environmental Modelling & Software* 25(1): 51–65.

- Versteeg HK and Malalasekera W (2007) *An Introduction to Computational Fluid Dynamics: The Finite Volume Method*. Harlow: Pearson Education.
- Wieringa J (1992) Updating the Davenport roughness classification. *Journal of Wind Engineering and Industrial Aerodynamics* 41(1-3): 357–368.
- Wise AFE (1970) Wind effects due to groups of buildings. In: *Proceedings of the Royal Society Symposium Architectural Aerodynamics*, London.
- Xu X, Yang Q, Yoshida A, et al. (2017) Characteristics of pedestrian-level wind around super-tall buildings with various configurations. *Journal of Wind Engineering and Industrial Aerodynamics* 166: 61–73.
- Yoshie R, Mochida A, Tominaga Y, et al. (2007) Cooperative project for CFD prediction of pedestrian wind environment in the Architectural Institute of Japan. *Journal of Wind Engineering and Industrial Aerodynamics* 95(9-11): 1551–1578.
- Zhang CX (1994) Numerical predictions of turbulent recirculating flows with a κ - ϵ model. *Journal of Wind Engineering and Industrial Aerodynamics* 51(2): 177–201.

Appendix

Notation

Roman symbols

C_s	Roughness constant (0–1)
C_μ	Model constant (=0.09)
E	Empirical wall constant (9.793)
H, W, L	Building height, width, length (m)
K	Turbulence kinetic energy (m^2/s^2)
k_s	Equivalent sand-grain roughness height (m)
K	von Karman constant (0.40–0.42)
P	Density of air (kg/m^3)
P_k	Production of turbulent kinetic energy
P	Formal order of accuracy
R	Grid refinement factor
U	Mean wind speed (m/s)
U_{ref}	Reference wind speed (m/s)
u^*	ABL friction velocity (m/s)
y^+	Non-dimensional distance from the wall (-)
y_P	Center point (P) of the first cell
(z_0)	Aerodynamics roughness length (m)
Z	Height (m)
Z_{ref}	Reference height (m)
τ_w	Wall shear stress
Greek symbols	
A	Power law exponent
E	Turbulence dissipation rate (m^2/s^3)
Ω	Specific turbulence dissipation rate (m^2/s^3)
Φ	Velocity component
Σu	Root Mean Square (RMS) streamwise velocity fluctuation amplitude (m/s)
M	Dynamic viscosity of air ($kg/m/s$)